Robust Prediction of Clinical Deep Brain Stimulation Target Structures via the Estimation of Influential High-Field MR Atlases

Jinyoung Kim[1], Yuval Duchin[2], Hyunsoo Kim[1,3], Jerrold Vitek[4], Noam Harel[2,5], and Guillermo Sapiro[1,3]

[1] Department of ECE, Duke University, Durham, NC, USA
[2] CMRR, University of Minnesota, Minneapolis, MN, USA
[3] Department of Biomedical Engineering, Duke University, Durham, NC, USA
[4] Department of Neurology, University of Minnesota, Minneapolis, MN, USA
[5] Department of Neurosurgery, University of Minnesota, Minneapolis, MN, USA

Abstract. This work introduces a robust framework for predicting Deep Brain Stimulation (DBS) target structures which are not identifiable on standard clinical MRI. While recent high-field MR imaging allows clear visualization of DBS target structures, such high-fields are not clinically available, and therefore DBS targeting needs to be performed on the standard clinical low contrast data. We first learn via regression models the shape relationships between DBS targets and their potential predictors from high-field (7 Tesla) MR training sets. A bagging procedure is utilized in the regression model, reducing the variability of learned dependencies. Then, given manually or automatically detected predictors on the clinical patient data, the target structure is predicted using the learned high quality information. Moreover, we derive a robust way to properly weight different training subsets, yielding higher accuracy when using an ensemble of predictions. The subthalamic nucleus (STN), the most common DBS target for Parkinson's disease, is used to exemplify within our framework. Experimental validation from Parkinson's patients shows that the proposed approach enables reliable prediction of the STN from the clinical 1.5T MR data.

1 Introduction

Deep brain stimulation (DBS) surgery is commonly used for symptom's treatment in neuro-degenerative diseases such as Parkinson's disease (PD). Precise placement of electrodes within crucial sub-cortical region (e.g., subthalamic nucleus (STN)) leads to successful DBS procedures [1].

Standard DBS targeting approaches today refer to anatomical information based on normalized atlases, particularly based on a single histology sample [1–3]. However, in such indirect methods, the variability in the position and size of the DBS targets needs to be further analyzed in the context of large populations for the reliability [2, 3]. To verify the target location, electrophysiological measurements, such as microelectrode recording (MER), that are lengthy and might result in increased risks for hemorrhage are required during surgery [1–3].

N. Navab et al. (Eds.): MICCAI 2015, Part II, LNCS 9350, pp. 587–594, 2015.
DOI: 10.1007/978-3-319-24571-3_70

Direct visualization and localization of the targets on the *individual* patient are needed for reliable, safe, and time-efficient DBS targeting. With advances in high-field MR (e.g., 7 Tesla (7T)), the superior contrast and high resolution imaging allow to directly identify and visualize the DBS targets, reducing the need for MER and other lengthy intra-operative burdensome steps [1, 3–6]. However, such high-fields are limited in clinical use, and thus the targets need to be localized on standard clinical low-field MR data. Unfortunately, clear visualization of DBS targets is not feasible with such standard clinical MRI protocols.

The aim of this work is to predict the location and shape of the DBS targets that are not normally identifiable on clinical 1.5T MRI. Recent studies have introduced regression approaches to estimate limited shape information within regions of interest from given predictors in the data [7–10]. In our scenario, it is hard to even manually localize DBS targets on the clinical low-field MRI, and thus it is still challenging to build high quality training data for such regression models from just the standard clinical data. In addition, the large variability of learned information from various training subsets might actually increase the uncertainty of the prediction. Furthermore, the influence of such subsets to prediction performance needs to be considered when developing reliable prediction.

In this work we propose a robust prediction framework for reliable DBS targeting on clinical low-field MRI, automatically learning dependencies between targets and predictors from more relevant high-field MR atlases. A key contribution of our work is how to learn shape relationships from high-field MR training sets applicable for DBS targeting on clinical low-field MRI. High quality information on the 7T MR training data is then transferred for DBS targeting onto the 1.5T MRI from a query patient. We apply bagging [11] in a regression model to predict location and shape of anatomical targets, reducing the variability (uncertainty) of learned relationships and obtaining confidence regions with high value for the DBS procedure. The training subsets producing the most accurate prediction are estimated via a machine learning approach. The robust prediction model and its application to STN targeting are described in the next section, followed by experiments demonstrating that our proposed framework enables reliable prediction of the STN on clinical 1.5T MRI for Parkinson's patients.

2 Methods

Target structures and their predictors, segmented from high quality 7T MR training sets, are first registered onto the 1.5T MRI pairs of the same subject [12], and then non-linearly registered onto the 1.5T MRI of a different subject [13]. This enables us to correctly extract features of predictors for the 1.5T MR test data from 7T MR training shapes on the common coordinate space.

2.1 Ensemble Prediction

Our approach uses an ensemble of predictions exploiting learned dependencies between targets and predictors from random subsets of 7T MR training sets. We provide now details on the approach.

Pose and Shape Parameterization. Three dimensional (3D) shapes of predictor and target structures for M random subsets of N 7T MR training sets are represented as the coordinates of surface points, $\mathbb{x}_{i,j} \in \mathbb{R}^{n_\mathrm{x} \times 3}$ and $\mathbb{y}_{i,j} \in \mathbb{R}^{n_\mathrm{y} \times 3}$, respectively, for $i \in \{1, ..., N\}$ and $j \in \{1, ..., M\}$, where n_x and n_y are the number of surface points. To address the correspondence problem across training shapes, we adopt a recent minimum description length based method [14].

The Procrustes analysis [15] is performed on predictors $\mathbb{x}_{i,j}$ and targets $\mathbb{y}_{i,j}$ with respect to the mean of the surfaces, $m_{\mathbb{x}_j} = \frac{1}{N}\sum_{i=1}^{N} \mathbb{x}_{i,j}$ and $m_{\mathbb{y}_j} = \frac{1}{N}\sum_{i=1}^{N} \mathbb{y}_{i,j}$, respectively, across the 7T MR training sets, yielding pose parameter vectors $\gamma_{i,j}^{\mathrm{x}}$ and $\gamma_{i,j}^{\mathrm{y}}$ that include translations, scaling factors, and entries of a 3D rotation matrix. Poses for a predictor $\mathbb{x}^{(p)} \in \mathbb{R}^{n_\mathrm{x} \times 3}$ on the 1.5T MR test data are also parameterized as $\gamma_j^{\mathrm{x}^{(p)}}$ with respect to $m_{\mathbb{x}_j}$. Column vectors, $\bar{\mathbf{x}}_{i,j} \in \mathbb{R}^{3n_\mathrm{x}}$ and $\bar{\mathbf{y}}_{i,j} \in \mathbb{R}^{3n_\mathrm{y}}$ are obtained by concatenating all the coordinates for the surfaces aligned into $m_{\mathbb{x}_j}$ and $m_{\mathbb{y}_j}$, respectively and then modeled in lower dimensional space using kernel PCA in order to increase the predictive potential, considering non-linear relationships between training shapes [16]. Kernel principal components are denoted as $\beta_{i,j}^{\mathrm{x}}$ for predictors, $\beta_{i,j}^{\mathrm{y}}$ for targets on 7T MR training sets, and $\beta_j^{\mathrm{x}^{(p)}}$ for predictors on the 1.5T MR test data.

Bagging Regression. A bagging procedure [11] is applied in the partial least squares regression model [7, 9, 17] to learn shape relationships between targets and predictors, reducing their variability and providing confidence regions for the prediction. Regression coefficients $\mathbf{B}_{\mathrm{PLS},j}^{\beta}$ and $\mathbf{B}_{\mathrm{PLS},j}^{\gamma}$ for the shape parameters and poses, respectively, between targets and its predictors on the 7T MR training sets are obtained by a non-linear iterative partial least squares approach [17]. Given shape parameters $\beta_j^{\mathrm{x}^{(p)}}$ and poses $\gamma_j^{\mathrm{x}^{(p)}}$ for predictors on the 1.5T MR test data, $\beta_j^{\mathrm{y}^{(p)}}$ and $\gamma_j^{\mathrm{y}^{(p)}}$ for the target are predicted with the regression coefficients. Pre-image estimation of $\mathbb{y}_{\mathrm{est},j}^{(p)}$ in the original space from $\beta_j^{\mathrm{y}^{(p)}}$ is ill-posed since the kernel mapping is not invertible for non-linear functions [16]. We therefore utilize a reconstruction approach using the feature space distance [16].

After iterating the prediction for M random subsets, a final probability map is calculated as an ensemble of binary volumes, reconstructed from $\beta_j^{\mathrm{y}^{(p)}}$ and then transformed by $\gamma_j^{\mathrm{y}^{(p)}}$: $\mathrm{V}_{\mathrm{Pr}} = \frac{1}{M}\sum_{j=1}^{M} \mathrm{V}\left(\mathbb{y}_j^{(p)}\right)$. This, properly normalized, gives a probability interpretation of the prediction confidence.

2.2 Robust Prediction Model

Properly chosen subsets in the training data, for a particular patient, might contribute to further improvement of the prediction, reducing the bias from the learned information. To estimate the influence of such subsets in the prediction, we learn the dependency between features from random subsets and the prediction accuracy using a machine learning approach. Fig. 1 represents our robust prediction framework.

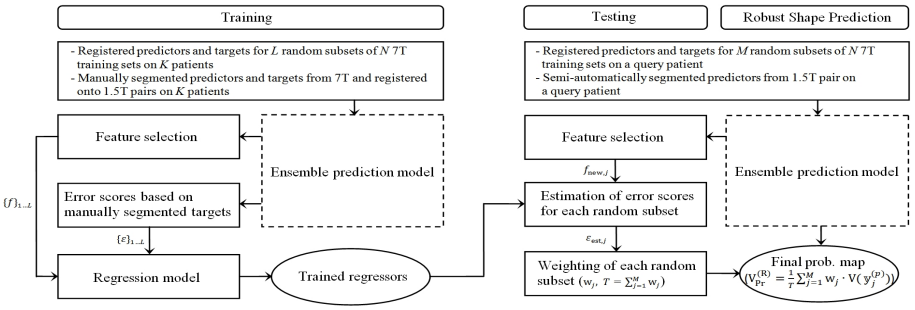

Fig. 1. Robust shape prediction framework.

Estimation of Influential Atlases. During the training, prediction using L random sets of N 7T MR training sets on K patients is performed, and pose parameters (i.e., $\mathbf{B}_{\mathrm{PLS}}^{\gamma}$, $\gamma^{\mathrm{x}^{(p)}}$, and $\gamma^{\mathrm{y}^{(p)}}$) are selected as features f, since poses for predictors and a predicted target are highly correlated to the prediction accuracy. Each prediction is then evaluated, measuring an error score ε that weighted averages distances from manually segmented targets,

$$\varepsilon = \mu_g(\epsilon_g/\delta_g) + \mu_l(\epsilon_l/\delta_l) + \mu_o(\epsilon_o/\delta_o) + \mu_v(\epsilon_v/\delta_v) + \mu_{\mathrm{DC}}((1-\mathrm{DC})/\delta_{\mathrm{DC}}), \quad (1)$$

where ϵ_g, ϵ_l, ϵ_o, and ϵ_v are errors between each prediction and manual segmentation, respectively, for centers, radii, orientation angles, and volumes. DC is the coefficients $\left(\left(2\left|\mathrm{V}^{(p)} \bigcap \mathrm{V}^{(m)}\right|\right) / \left(\left|\mathrm{V}^{(p)}\right| + \left|\mathrm{V}^{(m)}\right|\right)\right)$, where $\mathrm{V}^{(p)}$ and $\mathrm{V}^{(m)}$ are predicted and manual volumes, respectively. Also, μ and δ are weights and upper-bounds for corresponding errors. We set $\mu = [0.35\ 0.15\ 0.1\ 0.15\ 0.25]$ and $\delta = \left[1\mathrm{mm}\ 1\mathrm{mm}\ 30^{\circ}\ 50\mathrm{mm}^3\ 40\%\right]$, in this paper, weighting more ϵ_g and DC under acceptable error bounds for DBS targeting (ε <1).

To address the estimation problem of error scores, we utilize a regression forest model [10], which uses an ensemble of binary trees, learning non-linear mappings between features and error scores. Each tree optimally splits training samples, maximizing information gain among the distribution of error scores, and learned conditionals $p_t(\varepsilon \mid f)$ are stored on leaf nodes. Given a query patient and M random sets $s_{\mathrm{new},j}$ of training sets, each feature $f_{\mathrm{new},j}$ is pushed down on learned trees and stops at leaf nodes, resulting in $p_t(\varepsilon(s_{\mathrm{new},j}) \mid f_{\mathrm{new},j})$. The distributions are averaged over all N_{tree} trees, and finally error scores of each random subset are estimated: $\varepsilon_{\mathrm{est},j} = \arg\max_{\varepsilon_j} \left(\frac{1}{N_{\mathrm{tree}}} \sum_{t=1}^{N_{\mathrm{tree}}} p_t(\varepsilon(s_{\mathrm{new},j}) \mid f_{\mathrm{new},j})\right)$.

Weighted Ensemble of Prediction. For the M estimated error scores, normalized to [0 1], a weighting function is defined as $\mathrm{w}_j = \exp(-(\bar{\varepsilon}_{\mathrm{est},j})^3/\sigma^2)$, where σ is the mean of $\{\bar{\varepsilon}_{\mathrm{est}}\}$. This allows an ensemble of predictions, more weighting learned information from random subsets yielding lower error scores (i.e., more influential atlases for prediction). A final probability map on a query patient is computed by weighted averaging predictions from M random subsets: $\mathrm{V}_{\mathrm{Pr}}^{(\mathrm{R})} = \frac{1}{T}\sum_{j=1}^{M} \mathrm{w}_j \cdot \mathrm{V}(\mathrm{y}_j^{(p)})$, with $T = \sum_{j=1}^{M} \mathrm{w}_j$.

2.3 Application: Prediction of the STN for Clinical Targeting

We apply our proposed framework in DBS targeting problem of the STN which is critical for PD and potentially also for OCD [1, 6]. Predictors in sub-cortical region are introduced by considering the spatial adjacency (high correlation [7]) with the STN and the visibility on the 1.5T MRI. All such structures are easily detected on the 7T MRI [1, 4]. For comparison with the 1.5T MRI, see also [6].

3 Results

7T and 1.5T MR data sets were scanned from 46 patients. The 7T MR structures were manually segmented by anatomical experts, see also [4, 5], and registered onto the corresponding 1.5T MRI pairs, following [12]. We select 10 Parkinson's (PD) patients as 1.5T MR test sets. For each patient, 16 similar patients are chosen, and the corresponding 7T MR structures (registered onto the 1.5T MRIs) are then non-linearly transformed onto the 1.5T MR test data of the query patient using Advanced Normalization Tools [13]. We build training sets with size N=11 out of 16 patients and randomly generate M=10, 50, 100, 150, and 200 subsets. Predictors are automatically segmented on the 1.5T T_2W MRI of each query patient [5]. We perform forest training with N_{tree}=100, using L=18000 random subsets of N=11 training sets from K=9 PD patients, leaving one out and estimating error scores, given random subsets and predictors on 1 PD patient. Final probability maps are thresholded and then evaluated by calculating errors in (1). Fig. 2 shows average error scores of the prediction results and mean squared error (MSE) of estimated error scores $\{\bar{\varepsilon}_{\text{est}}\}$ from true ones for a different number of random subsets over the 10 PD patients. Average centroid distances and DC values for prediction results from 100 random subsets, as important measurements for DBS targeting, are also presented in Table 1.

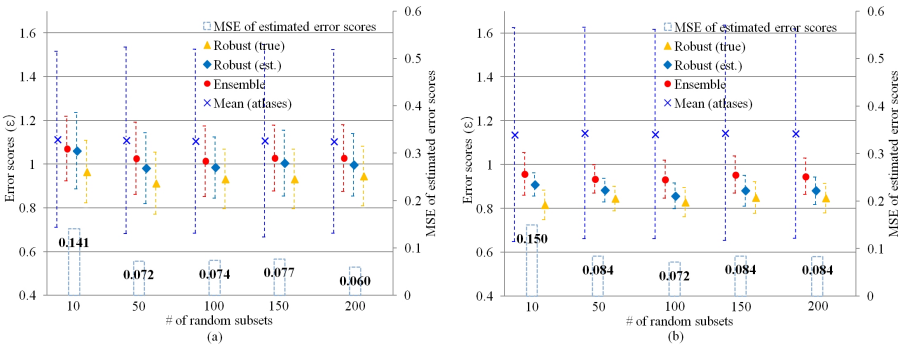

Fig. 2. Average error scores and their variances for 7T MR atlases based mean STN, ensemble prediction, and robust prediction (with estimated error scores and true ones), using a different number of random subsets over the 10 PD patients for (a) left and (b) right STN. Bars indicate MSE of estimated error scores from true ones.

Table 1. Average centroid distances, DC values, and their variances for 7T MR atlases based mean STN, ensemble prediction, and robust prediction using 100 random subsets.

		Mean(atlases)	Ensemble	Robust(est.)	Robust(true)
Left	ϵ_g(mm)	1.69±2.18	1.49±0.73	1.41±0.63	1.29±0.6
	DC(%)	54.7±5.4	60.4±2.1	60.9±2.2	62.4±2
Right	ϵ_g(mm)	1.76±2.61	1.34±0.51	1.16±0.38	1.1±0.4
	DC(%)	52.8±5.5	63.2±1.5	64.2±1.5	65.9±1.1

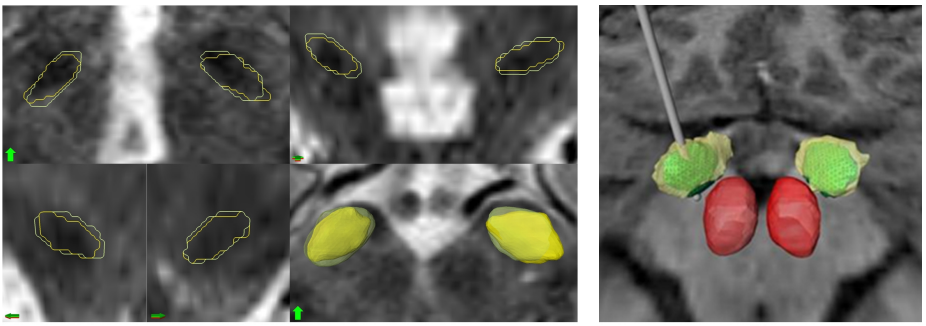

(a) (b)

Fig. 3. (a) Robust prediction with estimated error scores (green) using 100 random subsets on the 1.5T T_2W MRI from a specific PD patient, and the manually segmented STN (yellow). Contours on the axial plane (top left), the coronal plane (top right), and the sagittal plane (bottom left) are shown, respectively, followed by their 3D surfaces (bottom right). Arrows indicate anterior direction. (b) Post-operative placement of electrodes on the DBS motor sub-region within the predicted STN (green), along with the manually segmented STN (yellow) and the red nucleus (red) provided for validation and ease of 3D orienteering.

Overall prediction results on the 1.5T MR datasets are much closer to the manually segmented STN than the 7T MR atlases based mean STN (probability maps of binary volumes from $m_{\mathbf{y}_j}$), showing the prediction power of our proposed framework. Particularly, learned shape relationships are more effective to the prediction of the right STN, yielding lower error scores (the left STN have large variability over patients). Moreover, predictions are improved with the large number of random sets, showing the bagging effect (see differences in error scores between 10 and over 50 subsets, especially, for the left STN in Fig. 2).

We also observe that the proposed robust prediction with estimated error scores produces more accurate results than ensemble prediction (prediction results with true error scores are also presented for comparison). Particularly, for the number of subsets over 50, robust predictions are further improved, and centroid errors of the predicted right STN with 100 subsets are lowered over 10% (Table 1). This illustrates that random subsets with lower error scores, meaning more influential atlases for prediction, contribute to increasing the accuracy. Additionally, the smaller the number of random subsets, the higher the MSE

between estimated error scores and true ones. This might also explain why the robust prediction is more effective with large enough number of subsets.

Low DC (<70%) might be attributed to thresholding an ensemble of predictions. However, note that we provide the probability interpretation of confident target regions rather than the whole shape. Additionally, although our proposed robust prediction shows improvement in error scores, centroid distance, and DC, for its practical use, it is required to validate if the prediction results are clinically acceptable. For that purpose, we qualitatively investigated if small sub-regions (posterior-lateral) of the predictions are completely inside the DBS target subregion (e.g., motor territory) of true STN and observed that 95% of the predictions (19 out of 20 – both sides of 10 patients) hit the target regions. Fig. 3 shows that our proposed robust prediction provides confident targeting regions on the 1.5T MRI from a PD patient, with clinically feasible measurements (ε=0.48 and 0.58, ϵ_g=0.27mm and 0.76mm, and DC=76.8% and 78.2% for left and right STN, respectively). The DBS lead into the motor region of the STN is accurately placed on sub-regions within our prediction (Fig. 3(b)).

4 Conclusion

We presented a shape prediction framework that enables direct targeting for Deep Brain Stimulation (DBS) surgery based on standard clinical MR images. This is obtained by ensemble learning spatial relationships between DBS targets and their predictors using highly detailed information from 7T MR imaging. We proposed a robust way to improve the prediction, estimating the contribution of different training subsets. Given each subset on a patient, the influence to the prediction is estimated based on error scores and weighted to produce the final accurate and robust prediction.

Experimental results validated that our approach can fully predict the STN on the clinical 1.5T MRI from PD patients, where it is not possible to directly identify it. Ensemble prediction results were much closer to the ground truth manually segmented STN from the 7T MRI than atlases based mean STN, showing the predictive potential and further improved with large number of training subsets, reducing the variability of the learned information. The proposed robust prediction showed more accurate results, considering the contribution of random subsets to the prediction accuracy that leads to bias reduction from atlases. Moreover, small posterior-lateral regions of the predictions provided clinically acceptable localization of the patient-specific DBS lead within true STN.

Accurate estimation of error scores as a measure for the influence to prediction produces more reliable prediction, and thus relevant features need to be further investigated. Additionally, improving quality of predictors on the 1.5T MRI might considerably increase the prediction accuracy. Our ongoing efforts include the study of additional potential predictors and applications to other DBS targets (e.g., internal globus pallidus and ventralis intermedius). Ultimately, to reduce the need for MER in practice, it also remains challenging to minimize registration errors within our prediction framework and validate the manually segmented STN from 7T MRI using the MER mapping to address brain shift.

References

1. Abosch, A., Yacoub, E., Ugurbil, K., Harel, N.: An assessment of current brain targets for deep brain stimulation surgery with susceptibility weighted imaging at 7 tesla. Neurosurgery 67(6), 1745–1756 (2010)
2. Daniluk, S., Davies, K.G., Ellias, S.A., Novak, P., Nazzaro, J.M.: Asssessment of the variability in the anatomical position and size of the subthalamic nucleus among patients with advanced Parkinsons disease using magnetic resonance imaging. Acta Neurochirurgica 152(2), 201–210 (2010)
3. Xiao, Y., Jannin, P., D'Albis, T., Guizard, N., Haegelen, C., Lalys, F., Vérin, M., Collins, D.L.: Investigation of Morphometric Variability of Subthalamic Nucleus, Red Nucleus, and Substantia Nigra in Advanced Parkinsons Disease Patients Using Automatic Segmentation and PCA-Based Analysis. Human Brain Mapping 35(9), 4330–4344 (2014)
4. Lenglet, C., Abosch, A., Yacoub, E., De Martino, F., Sapiro, G., Harel, N.: Comprehensive in vivo mapping of the human basal ganglia and thalamic connectome in individuals using 7T MRI. PLoS One 7, e29153 (2012)
5. Kim, J., Lenglet, C., Duchin, Y., Sapiro, G., Harel, N.: Semiautomatic segmentation of brain subcortical structures from high-field MRI. IEEE J. Biomed. Health Inform. 18(5), 1678–1695 (2014)
6. Cho, Z., Min, H., Oh, S., Han, J., Park, C., Chi, J., Kim, Y., Paek, S.H., Lozano, A.M., Lee, K.H.: Direct visualization of deep brain stimulation targets in Parkinson disease with the use of 7-tesla magnetic resonance imaging. J. Neurosurg. 113(3), 639–647 (2010)
7. Rao, A., Aljabar, P., Rueckert, D.: Hierarchical statistical shape analysis and prediction of sub-cortical brain structures. Med. Image Anal. 12(1), 55–68 (2008)
8. Baka, N., Metz, C., Schaap, M., Lelieveldt, B., Niessen, W., De Bruijne, M.: Comparison of shape regression methods under landmark position uncertainty. In: Fichtinger, G., Martel, A., Peters, T. (eds.) MICCAI 2011, Part II. LNCS, vol. 6892, pp. 434–441. Springer, Heidelberg (2011)
9. Blanc, R., Seiler, C., Szekely, G., Nolte, L., Reyes, M.: Statistical model based shape prediction from a combination of direct observations and various surrogates: Application to orthopaedic research. Med. Image Anal. 16(6), 1156–1166 (2012)
10. Criminisi, A., Robertson, D., Konukoglu, E., Shotton, J., Pathak, S., White, S., Siddiqui, K.: Regression forests for efficient anatomy detection and localization in computed tomography scans. Med. Image Anal. 17(8), 1293–1303 (2013)
11. Breiman, L.: Bagging predictors. Machine Learning 24(2), 123–140 (1996)
12. Duchin, Y., Abosch, A., Yacoub, E., Sapiro, G., Harel, N.: Feasibility of using ultrahigh field (7T) MRI for clinical surgical targeting. PLoS One 7, e37328 (2012)
13. Avants, B.B., Tustison, N.J., Song, G., Cook, P.A., Klein, A., Gee, J.C.: A reproducible evaluation of ANTs similarity metric performance in brain image registration. Neuroimage 54(3), 2033–2044 (2011)
14. Heimann, T., Wolf, I., Williams, T., Meinzer, H.: 3d active shape models using gradient descent optimization of description length. In: Christensen, G.E., Sonka, M. (eds.) IPMI 2005. LNCS, vol. 3565, pp. 566–577. Springer, Heidelberg (2005)
15. Cootes, T.F., Taylor, C.J., Cooper, D.H., Graham, J.: Active shape models – Their training and application. Comput. Vis. Image Understand 61(1), 38–59 (1995)
16. Rathi, Y., Dambreville, S., Tannenbaum, A.: Statistical shape analysis using kernel PCA. In: SPIE-IS&T Electronic Imaging (2010)
17. Abdi, H.: Partial least squares regression and projection on latent structure regression (PLS Regression). Wiley Interdiscip. Rev. Comp. Stat. 2(1), 97–106 (2010)